RSC Advances




ROYAL SOCIETY OF CHEMISTRY

www.rsc.org/advances

Cite this: DOI: 10.1039/c0xx00000x

www.rsc.org/xxxxxx

PAPER

# *In situ* synthesis of hierarchical mesoporous $Fe_3O_4$@C nanowires derived from coordination polymers for high-performance lithium-ion batteries

**Huanhuan Li,[a] Ruyu Xu,[a] Yaping Wang,*[b] Binbin Qian,[a] Hongbo Wang,[c] Long Chen,[a] Haobin Jiang,[a] Yulu Yang[a] and Yiyun Xu[a]**

***Received (in XXX, XXX) Xth XXXXXXXXX 20XX, Accepted Xth XXXXXXXXX 20XX***
**DOI: 10.1039/b000000x**

A facile two-step strategy is developed for *in situ* fabrication of hierarchical nanostructured $Fe_3O_4$@C mesoporous nanowires. Coordination polymers that served as a precursor and self-template are hydrothermal synthesized in the first step, and subsequently thermal treated in an inert atmosphere. Well-defined mesoporous nanowires that assembled by a large number of core-shell structured $Fe_3O_4$@C spherical particles with an ultrasmall and uniform size (~8 nm) are successfully obtained. As a proof-of-concept application, they are used as anode materials for lithium-ion batteries. These $Fe_3O_4$@C mesoporous nanowires exhibit excellent electrochemical performance with high reversible capacity, good cycling stability and rate capability. The remarkable electrochemical performance is due to the effective combination of ultrasmall and uniform $Fe_3O_4$ nanoparticles, mesoporous nanowire structures and carbon networks, which simultaneously supplies a high contact area, mitigates the volume change during the lithiation/delithiation process, and enhances the electronic conductivity.

## 1. Introduction

For the extensive applications of lithium-ion batteries (LIBs) in electric vehicles (HEV), plug-in hybrid electric vehicles (PHEV), and electric vehicles (EV), developoing electrode materials with high energy, high power densities, good cyclic stability and low cost are always an ongoing research focus. In the last two decades, a number of 3*d* transition metal oxides (such as NiO,[1,2] $Co_3O_4$,[3,4] $Fe_3O_4$[5,6] and $Fe_2O_3$[7,8] etc.) have been extensively investigated as potential anode materials for LIBs due to their higher theoretical capacities (~1000 mAh $g^{-1}$) and novel conversion mechanisms which involves the formation and decomposition of Li oxide ($Li_2O$), accompanying the reduction and oxidation of metal nanoparticles. In particular, $Fe_3O_4$ is attractive for its abundant, low-cost, biocompatible, and environmental benignity.[9-11] However, the intrinsic limits including low electrical conductivity and the severe volume change of $Fe_3O_4$ during lithium-ion insertion/extraction lead to unsatisfactory cycling stability and rate performance.

To circumvent these obstacles, one effective approach is to fabricate nanostructured $Fe_3O_4$.[12-16] Well-designed nanostructures not only shorten the path lengths for the transport of lithium-ions, which can improve its rate performance, but also provide flexible space to buffer the mechanical strain of lithium-ion insertion/extraction. In particular, designing a one-dimensional (1D) porous nanostructure is one of the most favorable strategies to improve the electrochemical performance of $Fe_3O_4$.[15,16] 1D nanostructures provide short transport path along the confined radial dimension, while the connected porous framework could not only allow for efficient active mass-electrolyte contact but also accommodate better the strains related to the structural transformation upon repeated $Li^+$ insertion/extraction. However, the high surface-to-volume ratio and large surface free energy of nanostructured electrode materials raises the risk of side reactions involving electrolyte decomposition between electrode and electrolyte, and the formation of thick solid electrolyte interphase (SEI) films, which consume much of the lithium supplied by the cathodes and thus lead to a high level of irreversibility (i.e., low columbic efficiency) and poor life cycle.[17] Therefore, fabricating nanostructured $Fe_3O_4$ with surface modifications should be considered. A promising way is to encapsulate nanostructured $Fe_3O_4$ by a carbon shell, which can not only effectively protect the active surfaces of nanostructures from electrolyte, but also significantly enhance the electronic conductivity of $Fe_3O_4$.[18-21] Accordingly, constructing a carbon-coated 1D porous nanostructure can provide large surface area, rapid lithium-ion transport, and excellent structure stability, resulting in outstanding lithium storage performance.[21] However, it is still a challenge to homogeneously disperse the high-surface-energy 1D porous nanostructures in a carbon matrix during preparation process.

Coordination polymers constructed from coordinate bonds between metal ions/clusters and multidentate organic ligands have attracted great attention and have undergone rapid development owing to their intriguing structures and potential applications.[22] The structures, sizes and morphologies of coordination polymers are diverse and controllable because of the

richness of the organic ligands and diversification of secondary building units.[23] Therefore, they are promising precursors or sacrificial templates to construct the morphology-inherited porous metal oxides.[24-26] Actually, coordination polymers often include metal-oxygen bond and carbon containing groups with ordered and repeated arrangement. Thus, it is possible to obtain homogeneously porous nanostructured transition metal oxides/carbon composites from thermal treatment of coordination polymers in an inert atmosphere.

Herein, we report a facile *in situ* synthesis strategy to fabricate hierarchical mesoporous $Fe_3O_4$@C nanowires from Fe-based coordination polymers. The detailed synthesis procedures are described in the experimental section and the formation process is schematically illustrated in Fig. 1. In brief, $Fe^{2+}$ from dissolving $(NH_4)_2Fe(SO_4)_2{\cdot}6H_2O$ in distilled water will be coordinated with Nitrilotriacetic acid (NTA) during hydrothermal process to form nanowire structured Fe-NTA coordination polymers. During the *in situ* crystallization and carbonization process, core-shell $Fe_3O_4$@C nanoparticles are generated and assembled into mesoporous nanowires. This specific nanostructure encourages us to explore the actual applications in LIBs. As a result, mesoporous $Fe_3O_4$@C nanowires exhibit fascinating electrochemical performance, such as high reversible capacity, excellent cycling stability and good rate capability, when evaluated as an anode material for LIBs.

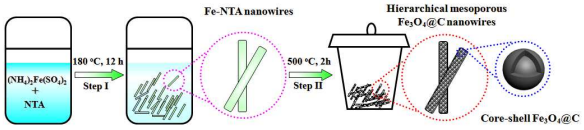


**Fig. 1** Schematic diagram of the preparation of hierarchical mesoporous $Fe_3O_4$@C nanowires

## 2. Experimental

### 2.1 Materials Synthesis

All the chemicals purchased were of reagent grade and used without further purification. $(NH_4)_2Fe(SO_4)_2{\cdot}6H_2O$ (J&K, 99%) and Nitrilotriacetic acid (Alfa Aesar, 98%) were used. In a typical procedure, 2.6 g of $(NH_4)_2Fe(SO_4)_2{\cdot}6H_2O$ and 0.6 g of Nitrilotriacetic acid (NTA) were added to 40 ml distilled water with vigorous stirring. The mixture was then transferred into a 50 ml Teflon-lined autoclave, which was gradually heated to 180 °C and maintained at this temperature for 12 h. After cooling down naturally, the white products were centrifuged, washed, vacuum-dried, and calcined at 500 °C in Ar for 2 h to obtain the hierarchical mesoporous $Fe_3O_4$@C nanowires.

### 2.2 Characterization

The structures of the as-prepared materials were determined by X-ray powder diffraction (XRD, Rigaku D/Max-2500 with Cu Kα radiation). The morphologies were evaluated by filed-emission scanning electron microscopy (SEM, JEOL JSM-6700F field emission), transmission electron microscopy (TEM) and high-resolution transmission electron microscopy (HRTEM) on a JEOL JEM-2100 transmission electron microscope. The thermal performance of the Fe-NTA coordination polymers has been evaluated on a NETZSCH STA 449C instrument under Ar (99.999%) atmosphere at a heating rate of 10 °C $min^{-1}$. Fourier transform infrared spectroscopy (FTIR) spectra of Fe-NTA and pure NTA were determined by a FTIR-650 spectrometer (Bruker Tensor 27). Nitrogen adsorption/desorption measurements (NOVA 2200e, Quantachrome Instruments) were performed to characterize the Brunner–Emmet–Teller (BET) specific surface areas and porous instincts of the obtained $Fe_3O_4$@C nanowires. Carbon analyses of the hierarchical mesoporous $Fe_3O_4$@C nanowires were performed on a Perkin-Elmer 240C elemental analyzer.

### 2.3 Electrochemical Tests

The electrochemical tests were carried out with CR2032-type coin cells. The working electrode was prepared by mixing 70 wt% active materials (the obtained hierarchical mesoporous $Fe_3O_4$@C nanowires), 20 wt% carbon black (Super P) and 10 wt% polyvinylidene fluoride (PVDF) dissolved in N-methylpyrrolidinone (NMP). The formed slurry was coated onto a copper foil and dried at 80 °C for 12 h. Then, the electrode was assembled into coin cell (CR2032) with a Celgard separator membrane and lithium metal as the counter and reference electrode in an argon-filled (99.999%) glovebox. The electrolyte was 1 mol $L^{-1}$ $LiPF_6$ in ethylene carbonate (EC)-diethyl carbonate (DEC)-ethylmethyl carbonate (EMC) (1:1:1 vol %). The galvanostatic charge-discharge and cycling performance measurements were carried out on LAND battery-test instruments (CT2001A) at various charge-discharge currents between 0.01 V and 3.0 V (vs. $Li/Li^+$). Cyclic voltammetry (CV) measurement was performed using a ZAHNER Zennium Electrochemical Workstation in a potential range of 0.1-3 V (vs. $Li^+/Li$) with the scan rate of 0.1 mV $s^{-1}$ at 25 °C.

## 3. Result and Discussions

### 3.1. Sample characterization

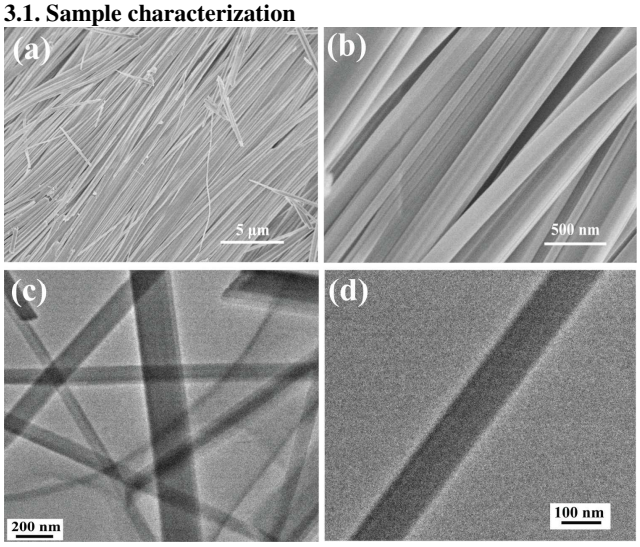


**Fig. 2** SEM (a,b) and TEM (c,d) images of Fe-NTA coordination polymers.

The morphologies of the Fe-NTA coordination polymers are characterized by scanning electron microscopy (SEM) and transmission electron microscopy (TEM). Fig. 2a and b show representative SEM images of polymers. It is clearly observed that a large quantity of highly aligned wire-like nanostructures

with lengths of several to tens of micrometers in Fig. 2a. A magnified view represents that the nanowires have smooth surfaces and are bundled with each other (Fig. 2b). Interestingly, the nanowire bundles can be disassembled into some single nanowires by ultrasonication for several minutes, as shown in the TEM images (Fig. 2c and d). The average diameter of the nanowire is about 150 nm.

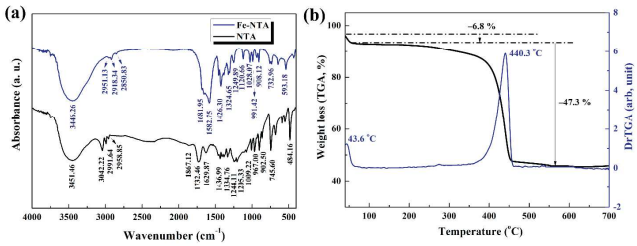


**Fig. 3** (a) Infrared (IR) spectras of NTA and Fe-NTA nanowires. (b) TGA and DTA curves of Fe-NTA nanowires.

The infrared (IR) spectras of NTA and Fe-NTA nanowires are shown in Fig. 3a. The bands ranging from 3100 to 2900 $cm^{-1}$ is related to the stretching vibration of C-H.[27] For NTA, the peaks are centered at 3042.22, 2991.64 and 2958.83 $cm^{-1}$. However, these peaks in Fe-NTA nanowires become very weak in intensity and shift to 2951.13, 2918.34 and 2850.83 $cm^{-1}$, respectively. This could be caused by the introduction of $Fe^{3+}$ coordination.[28] The band at 1732.46 $cm^{-1}$ for NTA is assigned to the stretching vibration of C=O. However, the C=O band disappears in Fe-NA nanowires, and a wide band composed of two peaks at 1681.95 $cm^{-1}$ and 1582.75 $cm^{-1}$ is observed instead, indicating the formation of -COOFe coordination group.[29]

The thermal stability of Fe-NTA coordination nanowires in Ar has been investigated by thermogravimetric analysis (TGA), as shown in Fig. 3b. The gradual mass loss of 6.8 wt% below 120 $^{o}$C is mainly due to the evaporation of absorbed water. When the temperature is increased to 440.3 $^{o}$C, there is a well-defined weight loss of about 47.3% occurred, which is due to the decomposition of Fe-NTA to $Fe_3O_4$@C. Therefore, the temperature for the calcination of the polymer nanowire precursor to $Fe_3O_4$@C is set at 500 $^{o}$C for 2 h to ensure the complete decomposition of Fe–NTA.

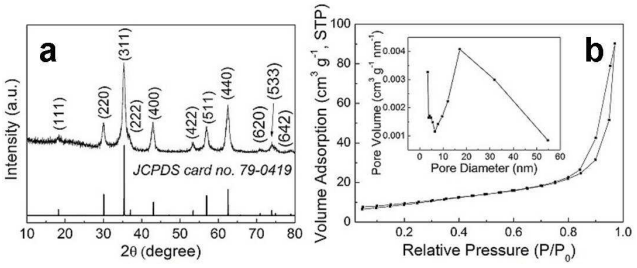


**Fig. 4** (a) XRD pattern of porous $Fe_3O_4$@C nanowires. Vertical bars below the pattern show the positions of all possible reflection peaks. The hkl labels are placed according to the reflection position. (b) $N_2$ adsorption/desorption isotherm curve of porous $Fe_3O_4$/C nanowires. Inset shows the pore size distribution.

The XRD pattern of the resulting $Fe_3O_4$@C product is shown in Fig. 4a. The sample presents the single phase that can be indexed to the cubic structure of $Fe_3O_4$ with a space group F*d-3m* (JCPDS file no. 79-0419). No other impurities are detected. In addition, the diffraction peaks are quite narrow, demonstrating the good crystallinity of sample. Moreover, elemental analysis results show that the amount of carbon is about 12.9 wt%. As no crystalline carbon (graphite) diffraction peaks are observed in the XRD pattern, it should be amorphous in the sample. Therefore, it is concluded that the precursor Fe–NTA nanowires are successfully transformed to $Fe_3O_4$@C.

To evaluate the permanent porosity of $Fe_3O_4$@C, $N_2$-sorption experiments were performed at 77 K. Fig. 4b shows the isotherm and corresponding Barrett-Joyner-Halenda (BJH) pore size distribution curves. The isotherm can be categorized as type IV curve, according to the IUPAC classification[30], with an H3 hysteresis loop located in the range 0.8–1.0 $p/p_0$, indicating a mesoporous characteristic. The Brunauer-Emmett-Teller (BET) from the $N_2$-sorption isotherm is 33.64 $m^2$ $g^{-1}$. Accordingly, the maximum $N_2$ adsorption of 90 $cm^3$ $g^{-1}$ gave a pore volume of 0.135 $cm^3$ $g^{-1}$. The pore-size distribution from the analysis of the $N_2$ isotherm at 77 K by using BJH method is around 17.12 nm.

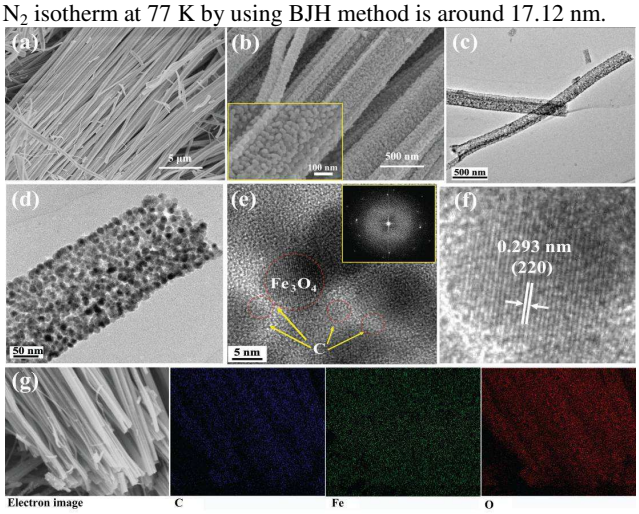


**Fig. 5** (a, b) SEM images of mesoporous $Fe_3O_4$@C nanowires. Inset shows HRSEM image of mesoporous $Fe_3O_4$@C nanowires. (c-d) TEM and (e) HRTEM image of mesoporous $Fe_3O_4$@C nanowires. The inset is the corresponding FFT pattern. (f) Atomic resolution lattice image of mesoporous $Fe_3O_4$@C nanowires. (g) Elemental mapping images.

SEM images of mesoporous $Fe_3O_4$@C are shown in Fig. 5a and b. At the first blush, it is obvious that the obtained product well inherits the morphology of Fe-NTA nanowires without structure collapse (Fig. 5a). However, the $Fe_3O_4$@C nanowires have hierarchical nanostructures in the enlarge view (Fig. 5b). It seems that several spherical particles assemble into a porous nanowire, as illustrated in the inset of Fig. 5b. TEM images (Fig. 5c and d) show that the prepared $Fe_3O_4$@C nanowires are composed of interconnected nanosized subunits with highly porous structure. Those subunits have a core-shell and polycrystalline structure with an ultrasmall and uniform size (~8 nm), as further illustrated in HRTEM image and fast Fourier transform (FFT) pattern (Fig. 5e and inset). The carbon network has an amorphous feature without lattice fringes. Moreover, the spacing of the planes is 0.293 nm (Fig. 5f), which matches well with the separations between the neighboring lattices of the (220)

planes of $Fe_3O_4$. Further, the elemental mapping images confirm the uniform distribution of C, Fe, and O in the mesoporous nanowires (Fig. 5g).

### 3.2. Electrochemical properties

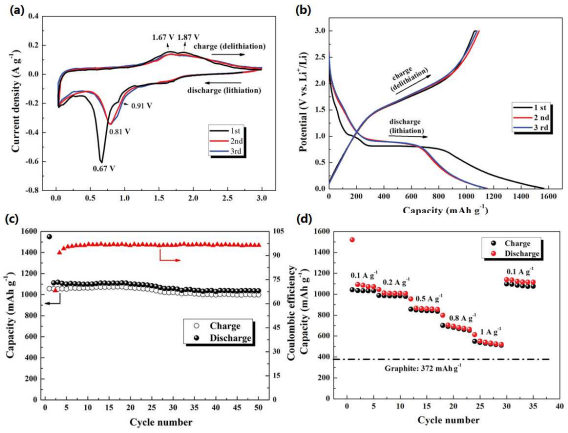


**Fig. 6** (a) CV profiles of hierarchical mesoporous $Fe_3O_4$@C nanowires at a voltage range of 0.01 to 3.0 V (vs $Li^+/Li$) and scan rate of 0.1 mV $s^{-1}$. (b) Typical first three charge/discharge profiles of hierarchical mesoporous $Fe_3O_4$@C nanowires. (c) Cyclic performance and (d) rate capability of hierarchical mesoporous $Fe_3O_4$@C nanowires.

Motivated by the advantages of hierarchical mesoporous $Fe_3O_4$@C nanowires as anode materials for lithium-ion battery, electrochemical measurements were carried out by using coin-type Li cells. Fig. 6a shows the first three cyclic voltammogram (CV) curves of the as-prepared $Fe_3O_4$@C electrode at room temperature. Two reduction peaks located at 0.91 and 0.67 V (vs $Li^+/Li$) can be found in the cathodic polarization process of the first cycle, which is usually attributed to the side reactions on the electrode surfaces and interfaces to form the solid-electrolyte interface (SEI), as well as the two steps of the lithiation reactions of $Fe_3O_4$ (step 1, $Fe_3O_4+xLi^++xe^-\leftrightarrow Li_xFe_3O_4$; and step 2, $Li_xFe_3O_4+(8-x)Li^++(8-x)e^-\leftrightarrow 4Li_2O+3Fe$).[31-33] During the subsequent anodic process, two oxidation peaks at around 1.67 and 1.87 V can be ascribed to the oxidation of Fe to $Fe_3O_4$. On successive scans, only one reduction peak can be detected at around 0.81 V, corresponding to the electrochemical reduction ($Fe_3O_4\rightarrow Fe$). Moreover, the peak intensity drops significantly, indicating the occurrence of irreversible reactions in the first cathodic scan. From then on, the CV curves are almost overlapped, which indicates the good reversibility of the electrochemical reactions. Therefore, it can be deduced that a stable SEI film forms on the surfaces and interfaces of carbon shells in the first cycle, which prevents the direct contact of encapsulated $Fe_3O_4$ nanoparticles with electrolyte and retains the structural integrity of $Fe_3O_4$ during subsequent charge-discharge cycles.[31-33]

Fig. 6b shows the first three discharge/charge voltage profiles of hierarchical mesoporous $Fe_3O_4$@C nanowires at a current density of 0.1 A $g^{-1}$ between 0.01 and 3.00 V. A total specific capacity of 1550 mAh $g^{-1}$ can be observed in the first discharge process, but a relative low reversible capacity of 1056 mAh $g^{-1}$ is achieved in the corresponding charge process, leading to an initial coulombic efficiency of around 70%. The excess capacity is due to the irreversible processes, including the inevitable formation of SEI and decomposition of electrolyte, which are common for transition metal oxides.[14,34-36] This also agrees well with the CV results. Moreover, the discharge voltage plateau at ~0.81 V in the first cycle is different from those of other cycles at ~0.9 V, also indicating the irreversible reactions in the first cycle. Furthermore, no obvious change in both charge and discharge profiles is observed during the subsequent cycles, showing excellent capacity retention.

The curve of capacity *versus* cycle number at a current density of 0.1 A $g^{-1}$ is shown in Fig. 6c. From the second cycle onward, hierarchical mesoporous $Fe_3O_4$@C nanowires exhibit excellent cycling stability. The reversible discharge capacity is about 1100 mAh $g^{-1}$, which can be retained at 1037 mAh $g^{-1}$ after 50 cycles. In addition, the Coulombic efficiency remains at about 97% after three cycles, suggesting a facile lithium insertion/extraction associated with efficient transport of ions and electrons in the electrode.

As the rate capability of hierarchical mesoporous $Fe_3O_4$@C nanowire electrode is also critical for practical applications, it was evaluated at various current densities from 0.1 to 1 A $g^{-1}$, as presented in Fig. 6d. The electrode delivers the average discharge capacities of 990, 850, 680 mAh $g^{-1}$ at 0.2, 0.5 and 0.8 A $g^{-1}$, respectively. Even at a high rate of 1 A $g^{-1}$, the reversible discharge capacity still retains at approximately 550 mAh $g^{-1}$, which is much higher than the theoretical capacity of graphite (372 mAh $g^{-1}$). More importantly, after the high-rate charge-discharge cycling, the discharge capacity can still be recovered to almost the same value by using a small density of 0.1 A $g^{-1}$, indicating the good reversibility of hierarchical mesoporous $Fe_3O_4$@C nanowires.

**Table 1** Comparison of electrochemical performance of hierarchical mesoporous $Fe_3O_4$@C nanowires with those $Fe_3O_4$/C composite anodes reported.

| Sample | Cycling performance | | Rate capability |
|---|---|---|---|
| | 1st discharge capacity | Cycling discharge capacity | |
| This work | 1550 mAh $g^{-1}$ at 0.1 A $g^{-1}$ | 1037 mAh $g^{-1}$ after 50 cycles | 550 mAh $g^{-1}$ at 1 A $g^{-1}$ |
| $Fe_3O_4$@N-rich Carbon Microspheres[37] | ~1400 mAh $g^{-1}$ at 0.0926 A $g^{-1}$ | 670 mAh $g^{-1}$ after 30 cycles | 363 mAh $g^{-1}$ at 0.463 A $g^{-1}$ |
| $Fe_3O_4$/C Microrods[38] | ~1200 mAh $g^{-1}$ at 0.2 A $g^{-1}$ | 650 mAh $g^{-1}$ after 100 cycles | 400 mAh $g^{-1}$ at 1 A $g^{-1}$ |
| $Fe_3O_4$/C[39] | 1221 mAh $g^{-1}$ at 0.1 A $g^{-1}$ | 856 mAh $g^{-1}$ after 60 cycles | 570 mAh $g^{-1}$ at 1 A $g^{-1}$ |
| $Fe_3O_4$/C[40] | 1600 mAh $g^{-1}$ at 0.05 A $g^{-1}$ | 610 mAh $g^{-1}$ after 100 cycles | 390 mAh $g^{-1}$ at 0.8 A $g^{-1}$ |
| Coaxial $Fe_3O_4$@C Hollow Particles[41] | 1318 mAh $g^{-1}$ at 1 A $g^{-1}$ | 864 mAh $g^{-1}$ after 50 cycles | 320 mAh $g^{-1}$ at 3 A $g^{-1}$ |
| C-$Fe_3O_4$ Nanospheres[42] | 1166 mAh $g^{-1}$ at 0.2 A $g^{-1}$ | 712 mAh $g^{-1}$ after 60 cycles | / |
| Macroporous $Fe_3O_4$/Carbon Microspheres[43] | 1258 mAh $g^{-1}$ at 2 A $g^{-1}$ | 1022 mAh $g^{-1}$ after 200 cycles | 621 mAh $g^{-1}$ at 9 A $g^{-1}$ |
| Mesoporous $Fe_3O_4$@C Nanospheres[44] | ~1300 mAh $g^{-1}$ at 0.1852 A $g^{-1}$ | 837 mAh $g^{-1}$ after 20 cycles | 642 mAh $g^{-1}$ at 0.926 A $g^{-1}$, 330 mAh $g^{-1}$ at 4.63 A $g^{-1}$ |

| | | | |
|---|---|---|---|
| $Fe_3O_4$@Carbon Nanorods[45] | 2085 mAh $g^{-1}$ at 0.926 A $g^{-1}$ | 808 mAh $g^{-1}$ after 100 cycles | / |
| Nitrogen-doped Carbon-coated $Fe_3O_4$[46] | ~1100 mAh $g^{-1}$ at 0.1 A $g^{-1}$ | 848 mAh $g^{-1}$ after 50 cycles | 485 mAh $g^{-1}$ at 1 A $g^{-1}$, 360 mAh $g^{-1}$ at 2 A $g^{-1}$ |
| Hollow Porous $Fe_3O_4$ beads-graphene[47] | 1233 mAh $g^{-1}$ at 0.1 A $g^{-1}$ | 1039 mAh $g^{-1}$ after 170 cycles | 396 mAh $g^{-1}$ at 1 A $g^{-1}$, 193 mAh $g^{-1}$ at 2 A $g^{-1}$ |

According to the results obtained, hierarchical mesoporous $Fe_3O_4$@C nanowires derived from Fe-NTA coordination polymers exhibit excellent electrochemical performance. These promising properties are better than most of the reported $Fe_3O_4$/C composite anodes (as compared in Table 1). [37-44] They might be related to their unique structural features in several aspects: (1) the building subunits with an ultrasmall and uniform size not only facilitate fast transport of lithium ions and electrons but also render a high surface area, which is critical to the rate capability. (2) the mesoporous nanowire structure could endure the volume expansion/contraction during the lithium ion insertion/extraction processes, leading to the attractive structure stability which can be reflected in the TEM images of cycled electrode (Fig. 7) and improving the cycling performance. (3) the carbon shells can protect the encapsulated $Fe_3O_4$ nanoparticles from directly contacting with the electrolyte and alleviate the side reactions on the interface between $Fe_3O_4$ and electrolyte, leading to structural and interfacial stabilization of $Fe_3O_4$ nanoparticles. (4) the carbon network interconnected the subunits constructs an efficient and continuous conductive net, resulting in good electrical conductivity and improving the rate capability.

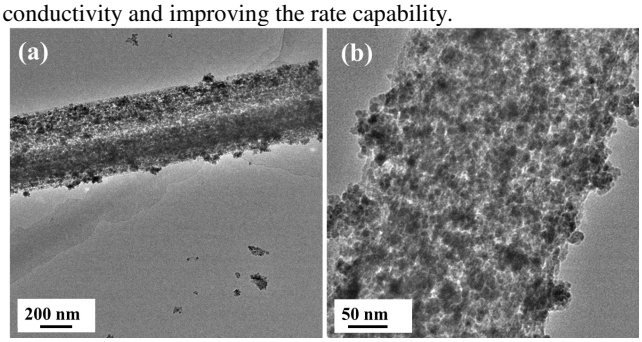


**Fig. 7** TEM images of hierarchical mesoporous $Fe_3O_4$@C nanowire electrode after 50 cycles.

## Conclusions

In summary, we have developed an efficient coordination polymer templating approach for *in situ* fabrication of hierarchical mesoporous $Fe_3O_4$@C nanowires. Lots of core-shell structured $Fe_3O_4$@C subunits with an ultrasmall and uniform size (~8 nm) were interconnected to construct mesoporous nanowires. The pore-size distribution was around 17.12 nm. When evaluated as an anode material for LIBs, those distinctive $Fe_3O_4$@C nanowires exhibited excellent electrochemical performance with high reversible capacity, excellent cycling stability and good rate capability. We believe that this low cost and convenient method could be extended to the fabrication of other metal oxide/carbon composites with well-designed hierarchical porous structures from specific coordination polymers, which may develop advanced electrodes in energy storage and conversion.

## Acknowledgment

This work was supported by the 863 Program (2012AA111401), the Natural Science Foundation of Jiangsu Province (BK2012293, BK20130482), the University Natural Science Research Project of Jiangsu Province (13KJB430008) and Research Foundation for Advanced Talents of Jiangsu University (13JDG071, 12JDG054) in China.

## Notes and references

[a] *Automotive Engineering Research Institue, Jiangsu University, 301 Xuefu road, Zhenjiang 212013, P. R. China.*
[b] *School of Material Science & Engineering, Jiangsu University, Zhenjiang 212013, P. R. China. Tel: 86 511 88797783; E-mail:wangyaping@ujs.edu.cn.*
[c] *China Aviation Lithium Battery Co. Ltd., Luoyang 471003, P. R. China.*

1 H. Liu, G. X. Wang, J. Liu, S. Z. Qiao and H. J. Ahn, *J. Mater. Chem.*, 2011, **21**, 3046.
2 Y. Xia, W. K. Zhang, Z. Xiao, H. Huang, H. J. Zeng, X. R. Chen, F. Chen, Y. P. Gan and X. Y. Tao, *J. Mater. Chem.*, 2012, **22**, 9209.
3 S. L. Xiong, J. S. Chen, X. W. Lou and H. C. Zeng, *Adv. Funct. Mater.*, 2012, **22**, 861.
4 N. Yan, L. Hu, Y. Li, Y. Wang, H. Zhong, X. Y. Hu, X. K. Kong and Q. W. Chen, *J. Phys. Chem. C*, 2012, **116**, 7227.
5 L. W. Ji, Z. K. Tan, T. R. Kuykendall, S. Aloni, S. D. Xun, E. Lin, V. Battaglia and Y. G. Zhang, *Phys. Chem. Chem. Phys.*, 2011, **13**, 7139.
6 T. Yoon, C. Chae, Y. K. Sun, X. Zhao, H. H. Kung and J. K. Lee, J. *Mater. Chem.*, 2011, **21**, 17325.
7 Y. Nuli, R. Zeng, P. Zhang, Z. P. Guo and H. K. Liu, *J. Power Sources*, 2008, **184**, 456.
8 Z. Y. Wang, D. Y. Luan, S. Madhavi, C. M. Li and X. W. Lou, *Chem. Commun.*, 2011, **47**, 8061.
9 S. Mitra, P. Poizot, A. Finke and J. M. Tarascon, *Adv. Funct. Mater.*, 2006, **16**, 2281.
10 P. L. Taberna, S. Mitra, P. Poizot, P. Simon and J. M. Tarascon, *Nat. Mater.*, 2006, **5**, 567.
11 D. Ho, X. Sun and S. Sun, *Acc. Chem. Res.*, 2011, **44**, 875.
12 Y. G. Guo, J. S. Hu and L. J. Wan, *Adv. Mater.*, 2008, **20**, 2878.
13 D. W. Su, H. J. Ahn and G. X. Wang, *J. Power Sources*, 2013, **244**, 742.
14 Y. Chen, H. Xia, L. Lu and J. M. Xue, *J. Mater. Chem.*, 2012, **22**, 5006.
15 Z. Xiao, Y. Xia, Z. H. Ren, Z. Y. Liu, G. Xu, C. Y. Chao, X. Li, G. Shen and G. R. Han, *J. Mater. Chem.*, 2012, **22**, 20566.
16 J. Wang, L. L. Li, C. L. Wong, L. F. Sun, Z. X. Shen and S. Madhavi, *RSC Adv.*, 2013, **3**, 15316.
17 Z. M. Cui, L. Y. Jiang, W. G. Song and Y. G. Guo, *Chem. Mater.*, 2009, **21**, 1162.
18 W. M. Zhang, X. L. Wu, J. S. Hu, Y. G. Guo, and L. J. Wan, *Adv. Funct. Mater.*, 2008, **18**, 3941.
19 C. N. He, S. Wu, N. Q. Zhao, C. S. Shi, E. Z. Liu and J. J. Li, *ACS Nano*, 2013, **7**, 4459.
20 L. Li, T. T. Wang, L. Y. Zhang, Z. M. Su, C. G. Wang and R. S. Wang, *Chem. Eur. J.*, 2012, **18**, 11417.
21 S. M. Yuan, J. X. Li, L. T. Yang, L. W. Su, L. Liu and Z. Zhou, *ACS Appl. Mater. Interfaces*, 2011, **3**, 705.
22 O. K. Farha and J. T. Hupp, *Acc. Chem. Res.*, 2010, **43**, 1166.
23 M. Sindoro, N. Yanai, A. Y. Jee and S. Granick, *Acc. Chem. Res.*, 2014, **47**, 459.
24 R. B. Wu, X. K. Qian, F. Yu, H. Liu, K. Zhou, J. Wei and Y. Z. Huang, *J. Mater. Chem. A*, 2013, **1**, 11126.

25 R. B. Wu, X. K. Qian, K. Zhou, J. Wei, J. Lou and P. M. Ajayan, *ACS Nano*, 2014, **8**, 6297.

26 X. D. Xu, R. G. Cao, S.Y. Jeong and J. Cho, *Nano lett.*, 2012, **12**, 4988.

27 L. B. Bellamy, *The Infrared Spectra of Complex Molecules*, John Wiley & Sons, New York, 1964, p. 13.

28 A. Weissberger, *Technique of Organic Chemistry*, Interscience, New York, 1967, Vol. IX, p. 341.

29 F. J. M. Rajabalee, *Spectrochim. Acta*, 1974, **30A**, 891.

30 K. S. W. Sing, D. H. Everett, R. A. W. Haul, L. Mouscou, R. A. Pierotti, J. Rouquerol and T. Siemieniewska, *Pure Appl. Chem.*, 1985, **57**, 603.

31 T. Zhu, J. S. Chen and X. W. Lou, *J. Phys. Chem. C*, 2011, **115**, 9814.

32 Z. C. Yang, J. G. Shen and L. A. Archer, *J. Mater. Chem.*, 2011, **21**, 11092.

33 Y. Z. Piao, H. S. Kim, Y. E. Sung and T. Hyeon, *Chem. Commun.*, 2010, **46**, 118.

34 S. H. Lee, S.-H. Yu, J. E. Lee, Ai. Jin, D. J. Lee, N. Lee, H. Jo, K. Shin,T.-Y. Ahn, Y.-W. Kim, H. Choe, Y.-E.Sung and T. Hyeon. *Nano Lett.*, 2013, **13**, 4249.

35 Z. Zeng, H. Zhao, J. Wang, P. Lv, T. Zhang and Q. Xia, *J. Power Sources*, 2014, **248**, 15.

36 H. Wu, N. Du, J. Wang, H. Zhang and D. Yang, *J. Power Sources*, 2014, **246**, 198.

37 C. X. Wang, G.J. Shao, Z. P. Ma, S. Liu,W. Song and J.J Song, *Electrochim. Acta*, 2014, **130**, 679.

38 Y. R. Wang, L. Zhang, X. H. Gao, L.Y. Mao, Y. Hu and X. W. Lou, *Small*, 2014, **10**, 2815.

39 P. P. Lv, H. L. Zhao, Z. P. Zeng, J. Wang, T. H. Zhang and X. W. Li, *J. Power Sources*, 2014, **259**, 92.

40 G. Chen, M. Zhou, J. Catanach, T. Liaw, L. Fei, S. G. Deng and H. M. Luo, *Nano Energy*, 2014, **8,** 126.

41 C. Lei, F. Han, Q. Sun, W. C. Li and A. H. Lu, *Chem. Eur. J.*, 2014, **20**, 139.

42 J. S. Chen, Y.M. Zhang and X. W. Lou, *ACS Appl. Mater. Interfaces*, 2011, **3**, 3276.

43 S. H. Choi, Y. N. Ko, K. Y. Jung and Y. C. Kang, *Chem. Eur. J.*, 2014, **20**, 11078.

44 J. Liu, Y. C. Zhou, F. Liu, C. P. Liu, J. B. Wang, Y. Pan and D. F. Xue, *RSC Adv.*, 2012, **2**, 2262.

45 T. Zhu, J. S. Chen and X. W. Lou, *J. Phys. Chem. C*, 2011, **115**, 9814.

46 Y. Ma, C. Zhang, G. Jia and J. Y. Lee, *J. Mater. Chem.*, 2012, **22**, 7845.

47 Y. Chen, B. H. Song, X. S. Tang, L. Lu and J. M. Xue, *J. Mater. Chem.*, 2012, **22**, 17656.